International Conference on Space Optics—ICSO 2022
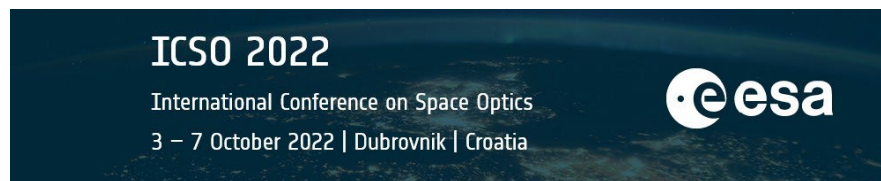
Dubrovnik, Croatia

3–7 October 2022

Edited by Kyriaki Minoglou, Nikos Karafolas, and Bruno Cugny,

Optical Calibration of the spectroradiometer based on a minispectrometer installed on the Solar Irradiance Sensor (SIS) for ExoMars'22 space mission

Optical Calibration of the spectroradiometer based on a mini-spectrometer installed on the Solar Irradiance Sensor (SIS) for ExoMars'22 space mission

E. García-Menéndez[*a], J. Jiménez-Martín[a], M. González-Guerrero Bartolomé[b], J. Martinez Oter[a], I. Arruego-Rodríguez[a]
[a] INTA - Instituto Nacional De Técnica Aeroespacial, Torrejón De Ardoz, Spain
[b] ISDEFE, as an external consultant at INTA

ABSTRACT

This work describes the procedure and results of the optical calibration of the spectroradiometer based on two mini-spectrometers installed on the Solar Irradiance Sensor (SIS'22) of the ExoMars'22 Radiation and Dust Sensor for Meteo package (RDM), in order to characterize the opto-electrical signal response.

The use of a lightweight, low-power and low-cost COTS (Commercial-of-the-Shelf) mini-spectrometer for planetary and space exploration opens up a large number of possibilities for payloads in current and future missions. These devices have to be qualified and calibrated under mission-specific environmental requirements that are beyond from the conditions for which they were designed. The main challenge of the calibration process is concerned with the extensive thermal range, from -145º C to 50º C, together with the angular response calibration by covering 90º zenith and 360º azimuth angles. This large thermal range, which exceeds the working range of the device, affects the offset level, the dark current signal and the spectral response by producing a spectral shift.

The mini-spectrometer is calibrated at INTA facilities considering all the possible configurations in terms of gain mode, acquisition mode and, integration time. The spectral response depends on several factors that must be characterized over the entire thermal range. The accuracy and precision are evaluated by detailed analyses based on the error propagation. This means to obtain the output signal under different conditions, which is important to determine information about the abundance of different gases in the atmosphere, the presence and size of particles and, dust events in the Mars surface.

Keywords: Solar Irradiance Sensor, ExoMars, spectrometer, optical calibration, Mars exploration

1. INTRODUCTION

The Solar Irradiance Sensor (SIS) is a radiometer of the METEO meteorological stations for the ExoMars 2022 Kazachok lander. It is a payload designed and developed by the INTA Payloads and Space Science Department, based on the previous multispectral and multichannel radiometers manufactured by the INTA team, like MetSIS for the Mars MetNet Precurssor Penetrator [1], the DREAMS-SIS for the ill-fated Shiaparelli lander of the ExoMars'16 mission [2]-[3] and, the Radiation and Dust Sensor (RDS) from the Mars Environmental Dynamics Analyzer (MEDA) weather station for the NASA/JPL Mars2020 Perseverance rover, which is operating from the red planet for more than 400 sols [6], [7].

All these instruments were designed to measure Mars'atmospheric properties [7] like the Aerosol Optical Depth (AOD) and the scattering phase function of the Martian dust. They can also detect clouds, ozone, even dust devils by using a combination of direct sky imaging and sky-pointing multi-wavelength and azimuthal measurements of diffuse light to capture the diurnal and seasonal evolution of these targets [8]. Comparing those observations at different sky sectors and wavelengths with radiative transfer simulations, dust and cloud scattering properties and gas abundances can be characterized and studied [9, 10]. Due to these previous radiometers were based on multichannel sensors composed by photodiodes, an additional challenge has been including two miniaturized spectrometers on this current instrument.

*garciamee@inta.es; phone (+34) 91 520 2166; http://www.inta.es

2. INSTRUMENT DESCRIPTION

The SIS′22 for the lander of the ExoMars′22 mission becomes the latest miniaturized radiometer developed at INTA planned to study the Mars atmospheric properties. It is interesting, but complicates the calibration and analysis processes, the fact that the design of the SIS'22 radiometer includes two different optical technologies: 17 discrete photodetectors and 2 mini-spectrometers. On the one hand, a set of 5 photodetectors with different optical band pass interferential filters are located on the top side of the instrument with a wavelength sensitive range from the ultraviolet to the near infrared. The other set of photodiodes are distributed in pairs on the SIS lateral faces, with the same UV and IR optical filters and tilted 70 degrees in the zenith coordinate. These detectors allow to continuously sample the incident light over the different azimuths in order to compare the brightness of the sky.

The main characteristics of the used spectrometers, the C12666MA HAMAMTASU mini-spectrometer, selected for this solar irradiance sensor, despite being COTS devices, they are considered as an ultra-compact spectrometer based on the micro-electro-mechanical-system (MEMS), obtaining a full spectrum with no moving parts. This mini-spectrometer is designed to allow simultaneous detection of multiple spectra. It is composed by the following elements:

-   Entrance slit: is an aperture through which the light to be measured is guided. This aperture size has significant effects on the optical characteristics such as spectral resolution and throughput.
-   Collimating lens: the light passing through the entrance slit spreads at a certain angle. The collimating lens collimates this slit-transmitted light and guides it onto the grating.
-   Grating: the grating separates the incident light into different wavelengths and lets the light at each wavelength pass through of reflect away at a different diffraction angle.
-   Focusing lens: the focusing lens forms an image of the light dispersed into wavelengths by the grating onto the linearly arranged pixels of the image sensor according to wavelength.
-   Image sensor: converts the optical signals, which are dispersed into wavelengths by the grating and focused by the focusing lens, into electrical signals and then outputs them.
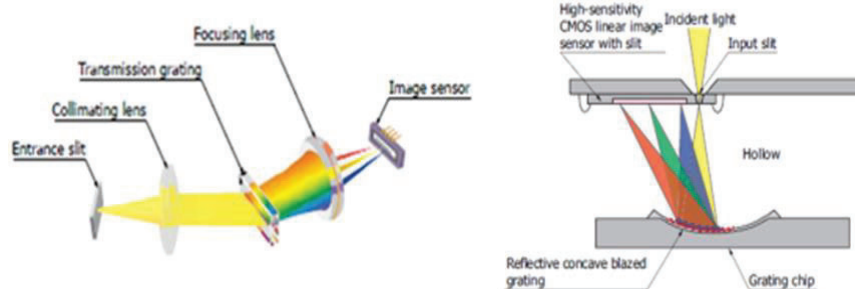

Figure 1. Mini-spectrometer composition detailed.

This mini-spectrometer has a working wavelength range between 340-780 nm with a field of view mask of 45° pointing to the zenith. According to the manufacturer, the mini-spectrometer has a spectral resolution of 15 nm and it is composed of 256 pixels.
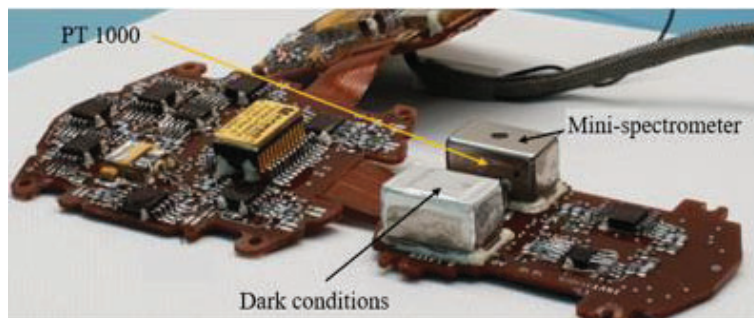

Figure 2. Mini-spectrometers and the internal PT1000 position for monitoring the temperature.

In addition, it has been included an internal PT1000 for monitoring the temperature during the thermal calibration tests. Figure 2 shows the internal location of the two mini-spectrometers and the thermal sensor inside the SIS'22 instrument. It is essential to introduce the thermal corrections to the optical signals, as it is explained in the following sections.

Figure 3 shows the distribution of 17 discrete photodetectors and two mini-spectrometers, with one of them covered and working in dark conditions. The main goal of this covered device is to obtain the dark signal, allowing to subtract the signal from the uncovered one. Additionally, this device will be used as a monitor of the displacement damage of the system due to particle radiation.
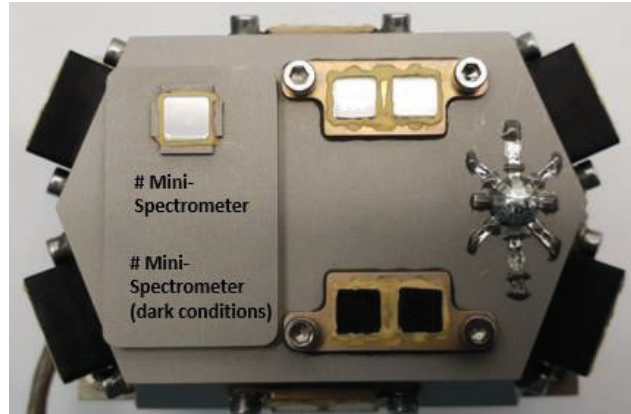

Figure 3. Flight Model Solar Irradiance Sensor (SIS'22) payload with both photodiodes and mini-spectrometers technologies.

The instrument can operate in 'differential' mode providing the subtraction of both covered and uncovered electrical signals or in 'single' mode, by providing only the one that receives light. This design improves reliability and allows the use of longer integration times, with the dark signal shortly affected.

Figure 4 shows the chosen reference system of SIS'22 where the instrument is presented on its azimuth ϕ, and zenith θ coordinates and how they vary.
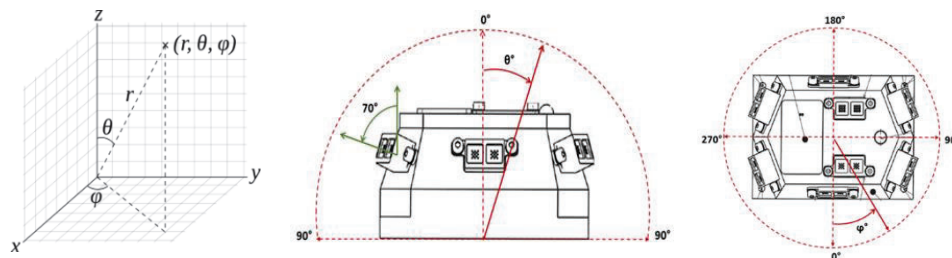

Figure 4. (a) Spherical coordinates reference system; (b) SIS zenith angle [θ]; (c) SIS azimuthal angle[ϕ].

The design requirements for every optical channel are collected in [11], measured in the reference system shown in Figure 4(a). The spectral throughput of the SIS optical channels depends on a combination of these elements:

-   Photodiodes and their spectral throughput. They are light-sensitive elements providing an electrical signal proportional to the incoming irradiance.
-   The interference filters modulate the spectral response into a band with specified limits. The area of the band where the light passes through is called the 'transmittance band' and the area where the light must be blocked is called the 'blocking band'. In practice, this element introduces losses in the transmittance band and is not fully opaque in the blocking band.
-   The field-of-view masks (FoV) modify the angular response by limiting the FoV of the photodiode, which only captures light from certain area of the sky. A 'tramittance zone' and a 'blocking zone' can be defined, in a similar way to those of the interference filters.

3. OPTICAL CALIBRATION PROCEDURE

The optical calibration procedure describes different tests, designed and developed to fully characterize the performance of the mini-spectrometer. The output signal based on an electrical response depends on the amount of incident light, the temperature at which the sensor is measuring, the angle of incidence of the light, and the mean throughput of the detector. Results display the performance of the mini-spectrometer in terms of integration time, gain mode and acquisition mode, to measure and study the atmosphere, dust size particles, brightness of the sky, optical depth, etc. depending on the illumination conditions on the surface of Mars.

3.1 General description of the SIS'22 mini-spectrometer calibration

The calibration model assumes that the light wavelength, the temperature, and the relative position of the radiative source can be considered as independent variables [12-17]. Therefore, the output signal generated for the mini-spectrometer can be expressed as follows:

$$I(T, \varphi, \theta, E_{Sun}) = ARF(\theta, \varphi) \cdot TRF(T) \cdot R^{\lambda_2}_{\lambda_1 \, Sun} \cdot E^{\lambda_2}_{\lambda_1 \, Sun} + offset(T) \qquad (1)$$

Where, the current given by the mini-spectrometer $I(T, \varphi, \theta, E_{Sun})$ depends on: $E^{\lambda_2}_{\lambda_1 \, Sun}$, is the Sun irradiance between λ_1 and λ_2 expressed in W/m^2; λ_1 and λ_2 are the initial and final wavelength of the band-pass filters defined in the previous section; ARF is the 'Angular Response Function', a dimensionless parameter between 0 and 1, that represents the signal dependence over the incoming light angle; TRF is the 'Thermal Response Function', another dimensionless parameter that represents the thermal dependence of the device response. TRF has been fixed to 1 at the mean work temperature of the instrument when the irradiance calibration test was performed; its responsivity, $R^{\lambda_2}_{\lambda_1 \, Sun}$, is the mean throughput between λ_1 and λ_2, under solar light spectrum irradiance and it is defined as:

$$R^{\lambda_2}_{\lambda_1} \left[A \cdot m^2 / W \right] = \frac{\int_0^\infty r(\lambda) \, E(\lambda) \, d\lambda}{\int_{\lambda_1}^{\lambda_2} E(\lambda) \, d\lambda} = \frac{\int_0^\infty r(\lambda) \, E(\lambda) \, d\lambda}{E^{\lambda_2}_{\lambda_1}} \qquad (1)$$

Finally, the $offset(T)$, expressed in amperes (A), is the sum of 'the offsets' produced by the conditioning electronics and by the dark current of the photodiode.

In all the calibration tests performed, the instrument provides a number of 'counts' obtained by the ADC (analogical-digital converter) proportional to the photocurrent, which can be expressed as:

$$\underbrace{S_{RDS}(counts)}_{Instrument\ Digital\ Signal} = \underbrace{K \left(\frac{Counts}{A} \right)}_{Constant\ that\ depends\ on\ the\ electronics} \cdot \underbrace{I(A)}_{Photodiode\ current} \qquad (3)$$

Then, it is possible to work directly with 'counts':

$$\overbrace{S_{RDS}(T, \varphi, \theta, E_{Sun})}^{\substack{Expressed\ in \\ [counts]}} = \overbrace{ARF(\theta, \varphi)}^{Dimensionless} \cdot \overbrace{TRF(T)}^{Dimensionless} \cdot \overbrace{R^{\lambda_2}_{\lambda_1 \, Sun}}^{\substack{Expressed\ in \\ [counts \cdot m^2 / W]}} \cdot \overbrace{E^{\lambda_2}_{\lambda_1 \, Sun}}^{\substack{Expressed\ in \\ [W/m^2]}} + \overbrace{offset(T)}^{\substack{Expressed\ in \\ [counts]}} \qquad (4)$$

Equation 4 shows the four terms that shall be characterized for the global calibration, but six independent characterizations are performed in order to calibrate the SIS'22 instrument. It is necessary two extra characterizations due to its spectral nature: the spectral response and the spectral TRF.

-   **Offset**: In dark conditions, the temperature is swept to cover the entire thermal range.
-   **TRF**: The optical power and the incidence angle of the light are fixed and only the temperature is made to change in order to evaluate the TRF under normal incidence of light.
-   **ARF**: The optical power and the temperature are fixed and only the light incidence angle is made to change in order to determine the angular response function.
-   **R**: The mean throughput under the normal incidence of sunlight spectrum.
-   **Spectral Response**: characterize the obtained spectra with the mini-spectrometer by measuring with Cd and Hg lam source and compare the pixels position of the maximum peaks found with a known certificated spectrum while the temperature is varying.
-   **Spectral TRF**: correction on the thermal displacement on the position of pixels due to variations of the diffraction grating due to the TRF test.

The calibration procedure includes different tests based on the mini-spectrometer main dependances as the thermal offset and dark current effect depending on the temperature, the thermal response (TRF), the spectral dependances, the angular response (ARF) depending on the angle of the incident light and, the main throughput (RSun) of the device, which depends on the irradiance level under normal incidence.

The SIS instrument has been calibrated at INTA facilities by using different optical ground support equipment, based on standard light sources as:

- Solar sun simulators: class A with respect to the spectral distribution, uniformity and temporal stability of irradiance [18].
- Specific discrete lamps as Hg-Cd and He-Ne, with similar spectrum emission as the mini-spectrometer under study.
- Optical neutral calibrated filters, to reduce the optical power irradiance from AM0 to a lower level, F50 and F35, with a transmittance of 50% and 35% respectively.
- Calibrated spectroradiometer, to measure the absolute irradiance spectrum.

3.2 Offset calibration: Electronic offset and dark current

The procedure to obtain the thermal offset calibration consists in measuring the signal from the mini-spectrometers, in dark conditions along the working thermal range defined. Then, these experimental data are fitted to a specific function defined by Equation (10), obtaining the offset as a function of the temperature, the gain mode, the acquisition mode and, the integration time. To obtain the final expression, it has to be considered that the offset signal per pixel has several contributions, as it is indicated in (5).

$$Offset_{i,j}[Counts] = \overbrace{b^{Ext}}^{\substack{External \\ electronic\ offset}} + \overbrace{b^{Int}_{CVC+ADC}}^{\substack{Internal \\ electronic\ offset}} + \overbrace{b^{Pixel}_{Dark}}^{\substack{Internal \\ "Dark\ current\ pixel\ signal"}} + photo\ signal \tag{5}$$

The contributions of the dark current depend on the integration time and the efficiency to transform to charge and also to voltage. So it is, the third term from (5) can be expressed as follows in (6):

$$Offset^{Pixel}_{Dark} = b^{Pixel}_{Dark} = \varepsilon_{i,j} \cdot R^{Q}_{i,j} \cdot \underbrace{\underbrace{T_{exp}[Counts]}_{Integration\ time} \cdot \overbrace{I^{Dark}_i}^{Dark\ current}}_{Charge\ generted\ in\ darkness} \tag{6}$$

On the other hand, the expression for the dark current can be written as:

$$I^{Dark}_i = A_{0_i} \cdot e^{(R_{0_i} \cdot T)} \tag{7}$$

So, the signal of each pixel given by (5) can be expressed like (8):

$$S_{i,j}[Counts] = \overbrace{\underbrace{b^{Ext}}_{\substack{External \\ Offset}} + \underbrace{b^{Int}_{CVC+ADC}}_{\substack{Offset\ of\ the \\ internal \\ electronic \\ mini-spectometer\ offset}} + \underbrace{\varepsilon_j \cdot R^Q_i \cdot T_{exp} \cdot I^{Dark}_i}_{\substack{Dark\ signal \\ of\ the\ CMOS}}}^{Signal\ in\ darkness} + \overbrace{\varepsilon_j \cdot R^Q_i \cdot T_{exp} \cdot R^Q_i \cdot R^{Optical}_i \cdot E}^{photo\ signal} \tag{8}$$

We are going to suppose that $\varepsilon_{i,j}$, $R^Q_{i,j}$, doesn't depend on the temperature and the offset of the internal electronic could be fit to a straight line like:

$$b^{Int}_{CVC+ADC} = m \cdot T + b \tag{9}$$

In darkness conditions, the signal of the mini-spectrometer is only the offset, operating (8), this expression depends only on the temperature, the gain, the acquisition mode and the integration time, it can be written as:

$$\boxed{S^{Dark}_{i,j}[Counts]} = \left(b^{Ext}_{High} + m^{Ext}_{High} \cdot \left(\boxed{T} - Tref\right)\right) \cdot \boxed{ch\_G} + \left(b^{Ext}_{Low} + m^{Ext}_{Low} \cdot \left(\boxed{T} - Tref\right) \cdot \left(1 - \boxed{ch_G}\right)\right) + \cdots$$

$$\cdots \left[b^{Int}_{k_i} + m^{Int}_{k_i} \cdot \left(\boxed{T} - Tref\right) + \left(A_{0_{k_i}} \cdot e^{\left(R_{0_i} \cdot \left(\boxed{T} - Tref\right)\right)}\right)\right] \cdot (1 + \overset{\overset{G=G_H= G'+1}{\uparrow}}{\widehat{G}} \cdot \boxed{ch_G}) \cdot \boxed{T_{exp}} \tag{10}$$

This mathematical model is based on the physical behavior between the mini-spectrometer measuring in darkness conditions and the other one which is uncovered, and can be expressed as follows in (11):

$$S_{Differential} = S_{Uncovered} - S_{Dark} + S_{0.5\,V}$$

$$S_{Single} = S_{Uncovered}$$

(11)

Based on (10) and (11), the data from every pixel have been fitted to the next equation (12), which allows to fully characterize the dark current signal obtained during the thermal calibration, considering all the configurations to facilitate and automatize the process.

$$S_{differential}[Counts] = S_{Single}[Counts] - S_{Dark}[Counts] =$$

$$\underbrace{\left(b_{High}^{Ext} + m_{High}^{Ext} \cdot (\boxed{T} - Tref)\right) \cdot ch\_G}_{\substack{S_{Single}\,External \\ Offset\,(HIGH\,gain)}} + \underbrace{(b_{Low}^{Ext} + m_{Low}^{Ext} \cdot (T - Tref) \cdot (1 - ch_G) + \cdots}_{\substack{S_{Single}\,External \\ Offset\,(LOW\,gain)}}$$

$$\overbrace{\cdots \left[\underbrace{b_{Single}^{Int} + m_{Single}^{Int} \cdot (T - Tref)}_{\substack{S_{Single}\,Internal \\ Offset\,signal}} + \underbrace{\left(A_{0\,Single} \cdot e^{\left(R_{0\,Single} \cdot (T - Tref)\right)}\right)}_{Pixel\,dark\,current\,Signal}\right]}^{Signal\,in\,darkness} \cdot (1 + ch_G \cdot G_{Single}) \cdot T_{exp} -$$

(12)

$$\underbrace{\left(b_{High}^{Ext} + m_{High}^{Ext} \cdot (\boxed{T} - Tref)\right) \cdot ch\_G}_{\substack{S_{Dark}\,External \\ Offset\,(HIGH\,gain)}} + \underbrace{(b_{Low}^{Ext} + m_{Low}^{Ext} \cdot (T - Tref) \cdot (1 - ch_G) + \cdots}_{\substack{S_{Dark}\,External \\ Offset\,(LOW\,gain)}}$$

$$\overbrace{\left[\underbrace{b_{Dark}^{Int} + m_{Dark}^{Int} \cdot (T - Tref)}_{\substack{S_{Dark}\,Internal \\ Offset\,signal}} + \underbrace{\left(A_{0\,Dark} \cdot e^{\left(R_{0\,Dark} \cdot (T - Tref)\right)}\right)}_{Pixel\,dark\,current\,Signal}\right]}^{Signal\,in\,darkness} \cdot (1 + ch_G \cdot G_{Dark}) \cdot ch_M \cdot T_{exp}$$

Where 'T' is the RAW temperature signal provide by the SIS'22, expressed in 'counts' obtained through the PT 1000 thermal channel. 'Tref' is the mean value temperature working, fixed at 51 980 counts. 'b' and 'm' are the parameters of a straight line, as it was shown in (9), it has to be considered the internal and the external contribution. 'A' and 'R' are the parameters of the exponential part of the dark current signal.

Figure 5 shows the set up for this test. The instrument is installed horizontally inside the Low/High temperature (LT/HT) thermal vacuum chamber. Then, the chamber is closed and carefully dried by making a high vacuum around 5 mbar. The quartz window gets covered to get dark conditions.

Figure 5. Set up for the thermal offset calibration test of the Flight Model Solar Irradiance Sensor (SIS'22). Thermal chamber opened (left) and closed (rigth).

The temperature inside the chamber is swept from room temperature to the maximum value of the thermal range. Then, it is fixed for stabilization and, afterwards, it is swept towards the minimum value of the range, where another stabilization is performed. Finally, the chamber is heated up again to ambient temperature. The thermal range used in this test was in the interval between 50 and -145 °C with a rate of change between 1 and 2 °C/min.

The number of parameters to fit is 19, as it was shown in equation (12), whereas the dependent variables are all the used configuration in the calibration test measurement: gain low (chG = 0), and high (chG = 1), mode of acquisition simple (chM = 0), and differential (chM = 1), integration time (Texp = 25, 2500 and 10 000 'counts') and the thermal temperature range 'T' defined. Before analyze the experimental data, the 0.5 V reference TIA (transimpedance amplifier) value has to be subtracted.

3.3 Thermal Response Function calibration (TRF)

The thermal response function, TRF, is the normalized photocurrent signal versus the temperature, that is, a factor that modifies the responsivity of a device depending on the temperature. TRF includes all factors that have an effect on the responsivity of the optical channels under study: changes in the transmittance of the optical parts, changes in the responsivity of the pixels and thermal drifts in the electronics of the instrument.

The TRF calibration test was carried out in the LT/HT thermal chamber under constant illumination by using a sun simulator as a light source. The mini-spectrometer is illuminated at a constant level of irradiance, to not saturate the photo at high temperatures, it has been used optical filters with a transmittance of 50% and 35%. The photocurrent signal from the pixels is intended to be measured simultaneously with the temperature by using different internal sensors. During the test, three extra thermocouples are used to monitor and control the temperature of the LT/HT chamber, the SIS unit and the interface. Figure 6 shows the set-up from this thermal calibration test, similar to the used in the Offset test.
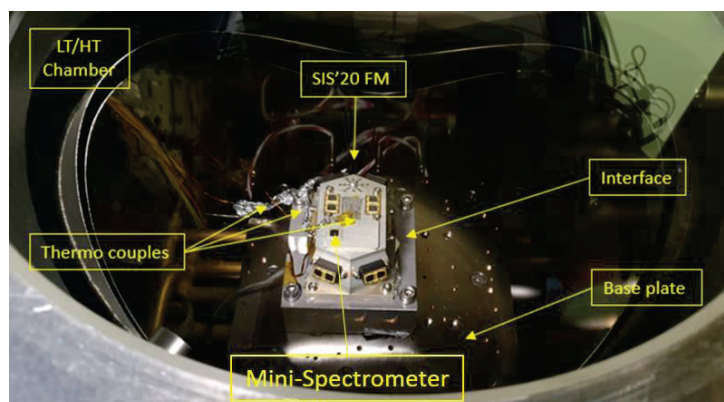
Figure 6. Set up for the thermal response function calibration test of the Flight Model Solar Irradiance Sensor (SIS'22).

It has been evaluated all the different possibilities of measuring with the mini-spectrometer depending on the chosen configuration. It is important to study all the possible ways of working, depending on the characteristics of the mini-spectrometer, especially sensitive to the integration time, operating mode, temperature and gain, to calibrate the device.

The obtained experimental data has to be corrected before the analysis. These corrections include the subtract of the 0.5 V reference value, the offset corrections obtained in previous section, eliminate the saturated data and corrections due to the thermal response behavior. All the measurements have been normalized to their corresponding integration time by dividing both magnitudes in 'counts'. Then the experimental data only depend on the gain configuration and the acquisition mode. Finally, the experimental data for each pixel has to be normalized to the mean work temperature value, in this case, the value is 51 980 'counts', the thermal range used in the analysis of the experimental data is between [30 000, 56 000] counts. Then, the data from every pixel has to be evaluated by using next equation 13:

$$TRF(T, M\_Adq) = \left(P5_S + P6_S \cdot (T - T_{ref}) + P7_S \cdot (T - T_{ref})^2\right) \cdot \left(1 - ch_{M\_Adq}\right)$$
$$+ \left(P5_D + P6_D \cdot (T - T_{ref}) + P7_D \cdot (T - T_{ref})^2\right) \cdot \left(ch_{M\_Adq}\right) \tag{13}$$

3.4 Spectral Response calibration

The main idea of this calibration test is to obtain the spectral response of the mini-spectrometer by analyses the measured spectrum in terms of identify the position of the pixel where the maximum values of the spectrum peaks are located. For the spectral response, it is needed to use a special source of light which has the peaks of its own spectrum coincident with the spectral wavelength range of the mini-spectrometer, between 340-780 nm. Figure 7 shows the set up for this calibration test, where it is needed the thermal chamber to control the temperature and a Hg-Cd lamp as a light source.
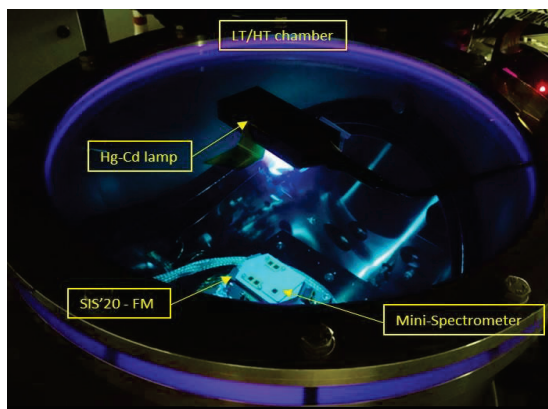
Figure 7. Set up for the spectral response calibration test of the FM SIS'22. It is shown the SIS installed inside the thermal chamber and the Hg-Cd lamp turned on over the mini-spectrometer.

To characterize the spectral response, the EGSE is configured to perform a measurement of the spectrum by using different configurations. Including single and differential acquisitions in both gains, nominal and high with the same value of integration time, fixed at 10000 counts.

Before analyze the experimental data, it is needed to subtract from them the TIA voltage reference value, to ensure the collected data are on the offset level. Then, the correction obtained in the offset analysis will be applied to the obtained measurements to correct the thermal offset dependencies.

The mathematical model used to identify the position of the pixels where the peaks of the spectrum are located is based on a 2D Gaussian function, as it is shown in the next equation 14.

$$Gaussian_{2D} = y0 + \left(\frac{A}{w \cdot \sqrt{\pi/2}}\right) \cdot e^{\left(-2 \cdot \left(\frac{x-xc}{w}\right)^2\right)} \tag{14}$$

This method allows to fit the measured spectrum with one Gaussian function per peak found in the experimental data and found the pixel position where the maximums have been found (Xc). The second step is to find the relation between the pixel positions and the corresponding value of the wavelength from the pattern spectrum of the Hg-Cd light source used. Figure 8 shows the calibration curves from NIST [¡**Error! No se encuentra el origen de la referencia.**], where it could be seen the correspondence between the value of the wavelength and the pixel where the peaks of different spectrums are located. Figure 8 shows the calibration curve given by the NIST (blue line), the calibration curve given by the manufacturer Hamamatsu (red line) and the emission lines measured with a reference mini-spectrometer C12880MA-109.
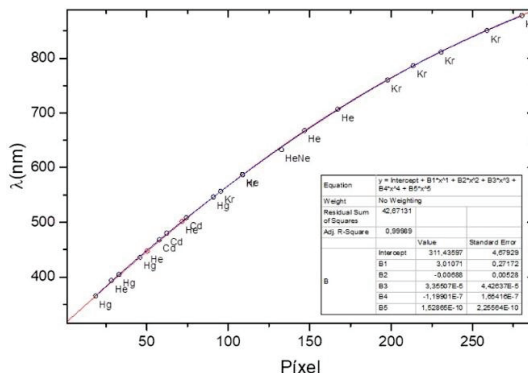
Figure 8. Calibrated curve form NIST (blue), from Hamamatsu (red) and emission lines (dots).

Once it has been identified the pixel position with the corresponding wavelength from the calibrated spectrum, these two magnitudes are represented as a curve and the next step is to obtain the characteristic parameters of the calibration equation given by the manufacturer, Hamamatsu, which is indicated in equation 15.

$$\lambda \ (nm) = \ A_0 + B_1 \cdot pixel + B_2 \cdot pixel^2 + B_3 \cdot pixel^3 + B_4 \cdot pixel^4 + B_5 \cdot pixel^5 \qquad (15)$$

Finally, the last step is to obtain the values of the wavelength by using the calibration equation 15 and both the values of the obtained parameters and each pixel position obtained in the test. The results will allow to estimate possible changes in the value of lambda for each position of the pixel where the peaks of the spectrum are located comparing the results with the given by the manufacturer.

3.5 Spectral Thermal Response Function calibration

This section described a thermal correction that should be applied before analyze the TRF calibration data. These effects appear on the position of the pixels caused by variations of the diffraction grating in the mini-spectrometer due to the TRF calibration test. After calibrate the spectral response in the previous section, the relation between the position where the maximum peaks of the spectrum are located and the corresponding wavelength was described and characterized. These effects have been seen when it has been measured spectrums at different temperatures. Figure 9 shows the spectral thermal effect over the measured spectrums at 7 different temperature values.
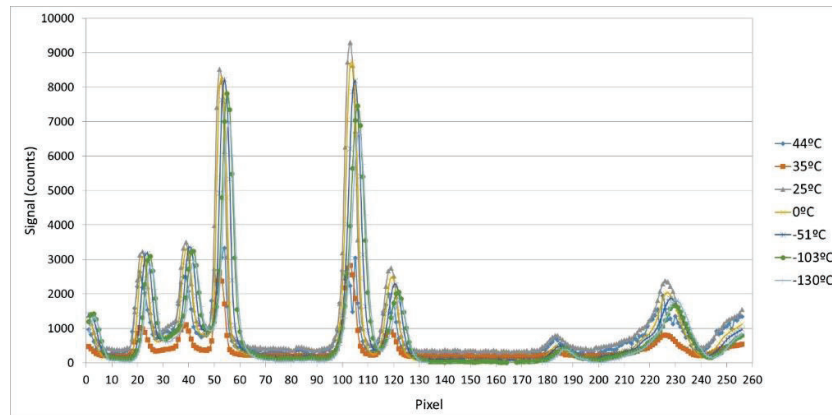
Figure 9. Measured spectra under similar configurations at different temperature values.

The position of the pixels seems to suffer a displacement to higher pixel position when the temperature is decreasing, these variations are around '4 pixels', which involves a thermal dependence in the spectral response which must be corrected. The goal of this analysis carried out on the experimental data is to obtain a mathematical expression which allows to related the variation of the wavelength displacement with the temperature.

The first step is to use (14) in order to obtain the position of the spectrum's peaks based on the lambda values given by NIST patterns. Then, with the obtained values and the calibration expression (15), a fitting is done in order to obtain the characteristics values of the parameters depending on the temperature. With these results, it is possible to stablish a relation between the temperature and each of the characteristic values, by representing each of them with the temperature, it is possible to obtain a mathematical expression for describing the thermal dependence.

After analyzed all the scenarios, it is chosen a reference value for the temperature at T = 35 °C. The rest of the data are normalized to this value, so it can be obtained the displacement on the pixel position of the peaks in terms of the temperature. Finally, the mathematical expression which allow to correct the spectral thermal displacement, give us an idea about the thermal sensitivity (wavelength/temperature) per pixel. The obtained expression for this correction is shown in (16).

$$\Delta \frac{nm}{°C} = -7.14 \cdot 10^{-8} - 1.26 \cdot 10^{-4} \tag{15}$$

3.6 Angular Response Function calibration

This function will give us information about the angular response of the mini-spectrometer by measuring the photocurrent when the irradiance level and the temperature are fixed and only the light incidence angle is changing for the zenith and azimuthal coordinates by using a high precision rotating setup.

Figure 10 shows the set up for this calibration test which has been performed in a 'dark room' in SPASOLAB facilities, at INTA. There, it is used a Xenom/Mercury lamp as a light source, placed approximately at a distance of 4.5 m from the system where the SIS unit is located. This distance will reduce the possible emission mismatches and allow us to consider the light that reaches the instrument as uniform and flat wave front.
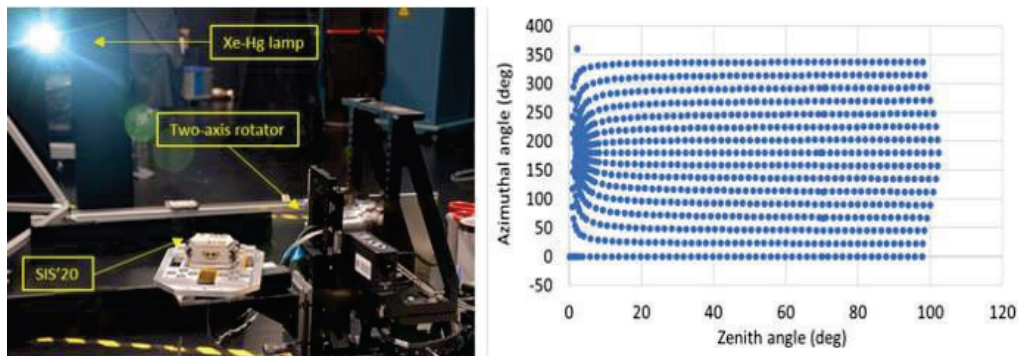
Figure 10. Set up for the ARF calibration test (left). The Xe/Hg lamp is pointing perpendicularly to the mini-spectrometer under study and the SIS'22 instrument is placed in a two-axis rotator system. Matrix of points to evaluate the ARF (right).

A careful alignment is required due to the FoV dimension of the device and its strong angular dependence. This is performed by using a mirror and bubble levels, its repeatability estimated is better than 0.2°. Once the SIS is well aligned with the top side poining normally to the light beam, the origin of coordinates of the rotator is reset to (0°,0°) in zenith and azimuthal angles. Then, the test is started by making a very detailed angular sweeps, from $\vartheta = [0°, 100°]$ and $\phi = [0°, 360°]$. Figure 10 shows, in the right side, the map of every pair of points considered in the calibration analysis. The instrument is commanded to measure under low and high gain configurations with 1024 cumulate measurements per each point of the defined matrix. Then, the EGSE recollects and provides the average of each measure. Before analyze the ARF results it is needed to apply the corresponding offset and TRF corrections to the obtained data.

There are some improvements with regard to previous calibrations tests performed with preceding instruments:

- The device is not totally hermetic and the light can penetrate in those angles for which the device should be blind by design, which is called the 'blocking zone'. This zone was found relevant when the Sun is outside the FoV and the irradiance over the SIS is mainly diffuse light. So, the 'blocking zone' beyond the FoV values has been characterized instead to be considered negligible as it was done in previous calibration procedures.
- The ARF has been fitted to an analytical equation instead of giving a matrix of smoothed experimental points. The ARF model is presented in this section and has two parts. The first one, for the characterization inside the FoV is based on the geometry of the FoV mask. The second one, which models the 'transition zone' and the 'blocking zone' is a composition of two functions with exponential decay.

In order to get the experimental data from the ARF calibration, the 0.5 V reference TIA value must be subtracted from the measurements, and offset, thermal and spectral corrections must be applied. Next to that, the experimental data are normalized to the minimum and maximum ARF values from each signal, as shown in equation 16:

- Minimum value: is the mean value from the experimental data filtered from zenith angles, between [90°, 100°], in the SIS reference system.

- Maximum value: is the mean value of the maximum values found.

$$ARF\ (\vartheta, \varphi) = \frac{(I\ (\theta, \varphi) - I_{\vartheta=90}^{\vartheta=100}}{I(\theta_\perp, \varphi_\perp) - I_{\vartheta=90}^{\vartheta=100}} = \frac{I\ (\theta, \varphi) - I_{min}}{I_{max} - I_{min}} \tag{16}$$

Next equation 17 presents the ARF model as a function of Zenith and Azimuth angles, in the SIS reference system.

Based on the FoV mask geometry

$$ARF'(\alpha) = z_0 + C' \cdot \overbrace{F_{FoV}(\alpha)} + \underbrace{A' \cdot F_2(\alpha) + AA' \cdot F_3(\alpha)} \tag{17}$$

Corrections to adjust the reflectivity
of the walls (the "tails") and the "blocking zone"

Where, the offset 'z0' of the ARF fitting is fixed to 0 due to the data normalization. The angle 'α' is referred to the SIS reference system. This angle is defined in the next equation 18, as the cross product between the coordinates from the pointing direction of the mini-spectrometer (x_θ, y_φ) and the coordinates of the incoming light pointing vector (θ, φ). Finally, C', A' and AA', are weights given to each function, to describe the relative influence of every parameter, and therefore, indicate when F3(α) takes significance, far away from the FoV angles.

$$\cos \alpha\ (\theta, \varphi) = \left| \left[\sin(x_\theta) \sin(\theta) [\cos(y_\varphi) \cos(\varphi) + \sin(y_\varphi) \cdot \sin(\varphi)] + \cos(x_\theta) \cdot \cos(\theta) \right] \times \sqrt{(aux_\theta)^2 + (aux_\varphi)^2} \right| \tag{18}$$

Regarding (18), 'θ' and 'φ' are the zenith and azimuthal angles of the light incident direction, 'aux_θ' and 'aux_φ' are two auxiliar variables based on the internal azimuthal angles between the light incidence angle and the pointing direction of the mini-spectrometer. This definition allows the FoV not being totally symmetric respect to its axis, allowing possible elliptical shape. 'aux_θ' and 'aux_φ' can be written as (19):

$$aux_\theta = W_\theta * \cos(rho + rotation)$$
$$aux_\varphi = W_\varphi * \sin(rho + rotation) \tag{19}$$

Next Figure 11 shows a scheme of these parameters, where 'W_θ' and 'W_φ' are the widths of the fitted function in each direction. Figure 11 (left) is a scheme of the angles as they are defined in (17) and (18), and Figure 11 (right) presents a particular situation when $W_\theta \neq W_\varphi$ and the optical response has an ellipitical shape in the FoV of the device.
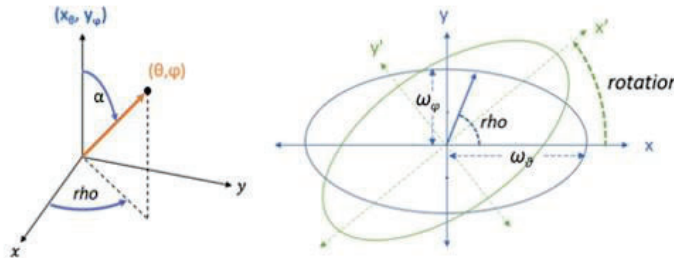

Figure 11. **(left)** α angle is a function of the light incoming angles (θ,φ) and the normal direction of the device (x_θ, y_φ) as given by the fitting. 'rho' angle as the projection of the incoming light angle in the working plane of the photodiodes. **(right)** Scheme of the 'rho' and 'rotation' angles considering an ellipse scenario when $W_\theta \neq W_\varphi$, and the possibility of being rotated respect to the SIS reference system.

The parameter 'rotation' is the 'inclination' of the FoV obtained in the fitting, given in radians. 'rho' is the angle formed by the projection of a vector with the direction of the incident light (θ, φ) on the plane perpendicular to the pointing direction of the FoV mask, (xθ, yφ), with the x-axis of that perpendicular plane. It can be observed in detail in Figure 11 (left).

Equation (17) is based on three functions depending on their domain. $F_{FoV}(\alpha)$ is a function that depends on the amplitude 'C', the radius, 'r', and the length, 'l', of the cylinders in the FoV mask. This equation (20), was composed assuming that the walls of the cylinders which form the collimator are totally black. Where, it has been considered 'r = 1.6 mm' and 'l = 2.5 mm'. Notice that (20) is not defined out of the FoV limits.

$$F_{FoV}(\alpha) = \left[2r^2 atan \left[\frac{\sqrt{4r^2 - l^2 tan^2 \alpha}}{l \tan \alpha} \right] - \frac{l \tan \alpha \sqrt{4r^2 - l^2 tan^2 \alpha}}{2} \right] \tag{20}$$

The other two functions of (17), F2(α) and F3(α), are presented in equation (21). On one side, F2(α) is a corrective factor for the adjustment of the reflectivity of the cylinder walls based on experimental data. It

helps to accurately model the 'tails' or 'transition zone' especially close to the FoV limit. On the other side, F3(α) fits the 'blocking zone' out of the FoV range, to simulate properly this angular dependence. Both expressions have the same form but different parameters.

$$F_i(\alpha) = \exp[-exp(-(\alpha - xc_i)/\omega_i) - ((\alpha - xc_i)/\omega_i) + 1] \quad \forall\, i = \{2, 3\} \tag{21}$$

Where 'xc_i' are the distance between the maximum value of each function and the maximum value of $F_{FoV}(\alpha)$, while 'ω_i' modulate the widths of these functions.

The correct way to use the ARF calibration model, after normalizing the data before the analysis (16), is to force the condition that ARF = 1 in all scenarios where light is perpendicularly on the device (α=0). This condition can be achieved by dividing the amplitude parameters from (17), C', A' and AA', by the maximum value of the ARF' evaluated in the pointing direction. With this normalization, the final ARF mathematical model is shown in equation 22.

$$ARF\ (\alpha) = z0 + \frac{C' \cdot F_{FoV}(\alpha) + A' \cdot F_2(\alpha) + AA' \cdot F_3(\alpha)}{ARF'_{Max}(\alpha = 0)} = z0 + C \cdot F_{FoV}(\alpha) + A \cdot F_2(\alpha) + AA \cdot F_3(\alpha) \tag{22}$$

Additionally, the ARF of the device, when it is working under diffuse irradiance must be also evaluated. The diffuse contribution can be obtained by integrating the ARF across a portion of the sky, to get the average of the ARF from that sector. This integral is defined in equation (23) as follows:

$$ARF\ diffuse = \frac{\int_0^\vartheta \int_0^\varphi ARF(\vartheta, \varphi)\partial\vartheta\partial\varphi}{\vartheta \cdot \varphi} \approx \frac{\sum_0^\vartheta \sum_0^\varphi ARF(\vartheta, \varphi) \cdot \Delta\vartheta \cdot \Delta\varphi}{N_\vartheta \cdot N_\varphi} \tag{23}$$

The ARF diffuse factor can be calculated to evaluate the incoming irradiance from the FoV of the mini-spectrometer, when $'\theta'$ and $'\varphi'$ angles are limited to the FoV values, or from the hole sky if $\theta = {}^\pi\!/_2$ and $\varphi = 2\pi$. The contribution of the diffuse radiation is especially significant in those sensors designed to work with the sunlight out of the FoV limits, when the irradiance on the SIS is relatively low.

3.7 Mean throughput calibration

The throughput is the relation between the irradiance level and the response of each pixel from the mini-spectrometer when the light is reaching normally the device. Hence, a sun simulator of known irradiance level has to be used and the SIS has to be mounted in a 2-axis rotator, parallel to the optical working plane. Figure 12 shows the set up for this calibration test and the matrix of points to evaluate the photosignal.
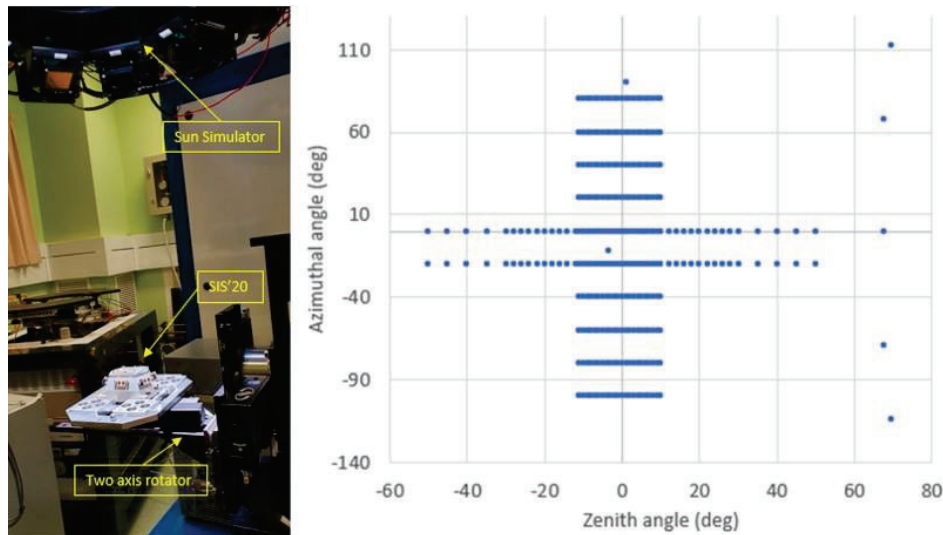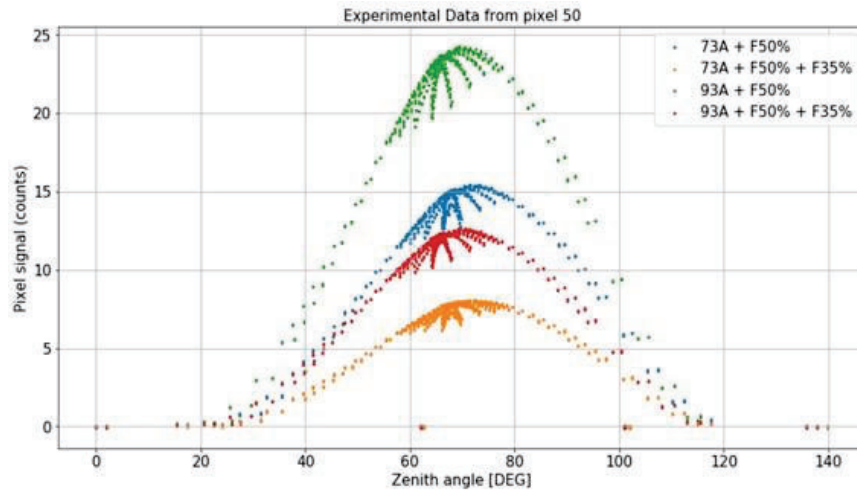

Figure 12. Set up for the mean throughput calibration test, with the SIS pointing perpendicularly to the beam light, installed in the two-axis rotator system (left). Matrix of points for the test (right).

Once the SIS unit is set and aligned, the azimuth and zenith angles from the rotator are reset to (0°, 0°) as the origin of coordinates. Then, each pixel response of the mini-spectrometer will be characterized by varying the azimuthal and zenith coordinates (ϑ, ϕ) in order to obtain the signal under normal incidence of light following the matrix of points indicated in Figure 12 (right).

The mini-spectrometer will be configured to measure under different configurations: nominal gain, in single and differential acquisition modes, and different integration times. In addition, four different calibrated optical filters and sun simulator configurations were used in the test to change the irradiance level:

- 73A + F50 %
- 73A + F50% + F35%
- 93A + F50%
- 93A + F50% + F35%

To correct and know the amount of irradiance reaching the instrument, the irradiance level has been integrated according to its wavelength range. This could be done by measuring the irradiance with a spectro-radiometer located in the same work plane of the instrument for each irradiance level used in the test. The obtained uncertainty value is 4.75 %, this value is the limit of the mini-Spectrometer SIS accuracy.

Before analyze the experimental data, it is important to apply the corresponding corrections. So it is, the subtraction of the TIA voltage reference value, the thermal offset correction and the TRF correction together with the spectral thermal response. There is another needed correction regarding to the AM0 spectrum. So it is, the measured spectra for each irradiance level have to be corrected by the AM0 factor. Figure 13 shows an example of the signal generated by pixel #50 under the four irradiance levels evaluated in the matrix of points shown in Figure 13.

Figure 13. Set up for the mean throughput calibration test, with the SIS pointing perpendicularly to the beam light, installed in the two-axis rotator system (left). Matrix of points for the test (right).

Having all of these ideas into account, the analyzed signal will be evaluated from the offset level around '0 counts', to the maximum level of 'counts' that each pixel generates which corresponds with the amplitude 'A' of the Gaussian 2D function, equation (24):

$$Z = Z_0 + A \cdot \exp\left(-\frac{1}{2}\left(\frac{x - ZE}{w_{ZE}}\right)^2 - \frac{1}{2}\left(\frac{y - AZ}{w_{AZ}}\right)^2\right) \tag{24}$$

Where, 'Z' is the measured signal of each pixel, 'Zo' is the offset level signal, 'A' is the amplitude, 'w_{ZE}' and 'w_{AZ}' are the widths of the simulated Gaussian in zenith and azimuthal directions, 'ZE' and 'AZ' are the zenith and azimuthal coordinates where the maximum of the signal is located.

Finally, to obtain the mean throughput, it is considered that the corrected signal of each channel is proportional to the irradiance level with a linear dependence, where the slope is the mean throughput value. This can be expressed as follows in equation (25):

$$\underbrace{\frac{S_{SIS}(E_{Sun})[Counts] - offset(T)}{ARF \cdot TRF}}_{\hat{Y}} = \underbrace{R^{\lambda_2}_{\lambda_1\,Sun}\left[counts \cdot W\big/m^2\right]}_{slope} \cdot \underbrace{E^{\lambda_2}_{\lambda_1\,Sun}\left[W\big/m^2\right]}_{\hat{X}} \tag{25}$$

4. RESULTS

This section collects the results from the calibration procedure explained along the previous sections. Due to the evaluated mini-spectrometer has 256 pixels to be calibrated, the results will be presented as examples from 1 or 2 different pixels and not with all of them to facilitate the comprehension of the shown plots. In addition, for the same reason it has not been included tables with the values of the characteristic parameters from all the used equations.

4.1 Thermal offset and dark current calibration

Figure 14 presents the experimental data from the thermal offset calibration test and the corresponding fitting – calculated by using equation (12) from the pixel #180. The first plot includes the experimental data (blue) and the fitting (orange), the picture in the bottom shows the residual from the fitting
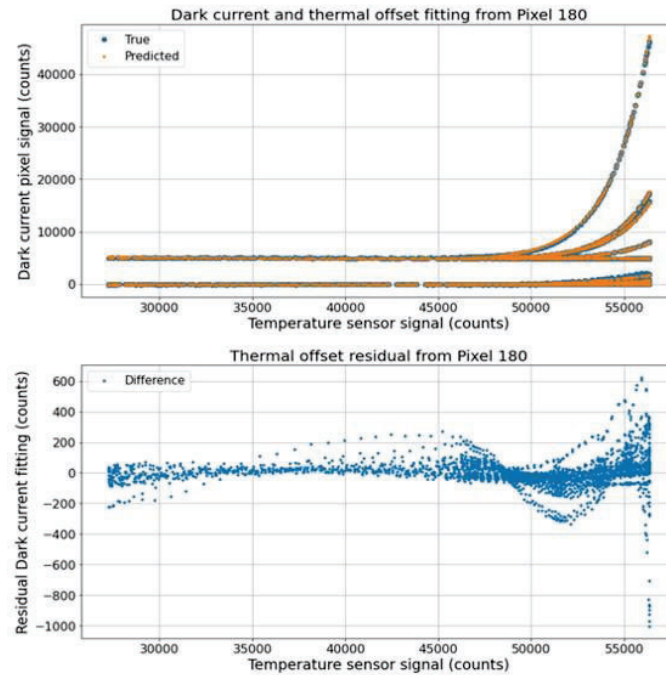
Figure 14. Experimental data (blue) and fitting (orange) from the thermal offset calibration analysis of pixel #180 (top). Residual from the fitting (bottom).

From figure 14 can be seen the dark current signal is appreciable beyond 50000 counts, and is dependant on the integration time value and gain configuration. In this example, the higher curve of dark current occurs when the integration time is 10000 counts under high gain scenario. In Figure 15 it has been Analyzed the residual in terms of gain and acquisition modes, and representing the residuals differentiating between the three values of integration time.
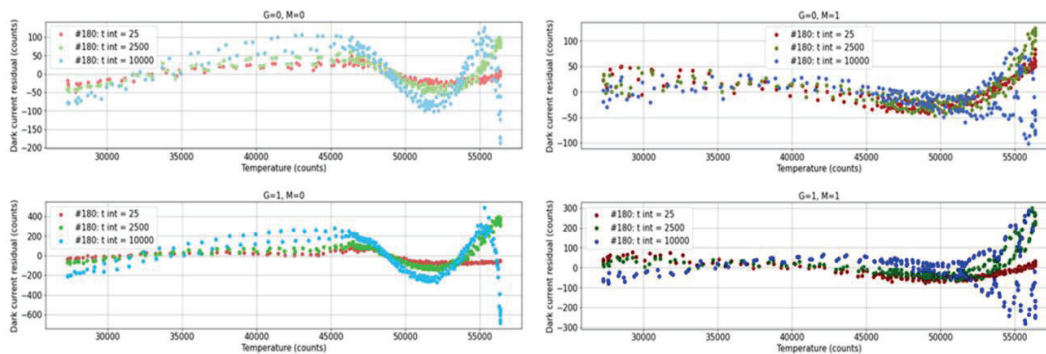

Figure 15. Residual at different integration times, 25 (red), 1500 (green) and 10000 (blue) counts. Gain and acquisition modes are: G=0, M=0 (first), G=0, M=1 (second), G=1, M=0 (third) and G=1, M=1 (fourth).

It is possible to determine that, the higher value of the obtained residual depending on the used configuration occurs when the mini-spectrometer is working in single acquisition mode (M=0) and under high gain configuration (G = 1).

Analyzing the residual of the fittings in two thermal ranges, considering cold (between 30 000 and 35 000 counts) and warm (between 48 000 and 52 000 counts) scenarios both of them at constant temperature and hence, independent of that variable, it is possible to obtain the corresponding electrical noise in dark conditions. Figure 16 presents the standard deviation of the statistical fits having evaluated all the 256 pixels separated in three equal intervals. The first range corresponds to the 'red' pixels from pixel #1 to pixel #85, the second range is the 'green' one, from pixel #86 to pixel #170, and the last one, the 'blue' range is from pixel #171 to pixel #256.
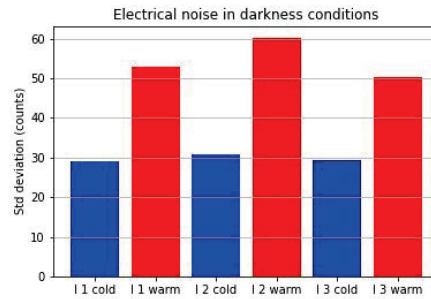
Figure 16. Standard deviation from the obtained dark signal residual fitting in two thermal ranges for the three integrated intervals of pixels studied.

4.2 Spectral Response calibration

The results from this calibration test include different analyses described in section 3.4. Figure 17 shows the obtained results and the relation from pixel position and peak (left) by using (14) and the parameters from (15) by using the NIST calibrated spectrum.

Pixel position	Peak 1	Peak 2	Peak 3	Peak 4	Peak 5	Peak 6	Peak 7	Peak 8	Peak 9
X_c	-0.15	21.70	38.61	52.14	102.83	118.53	183.15	225.91	254.77
Std X_c	2.00	0.05	0.06	0.02	0.02	0.07	1.20	0.31	2.33

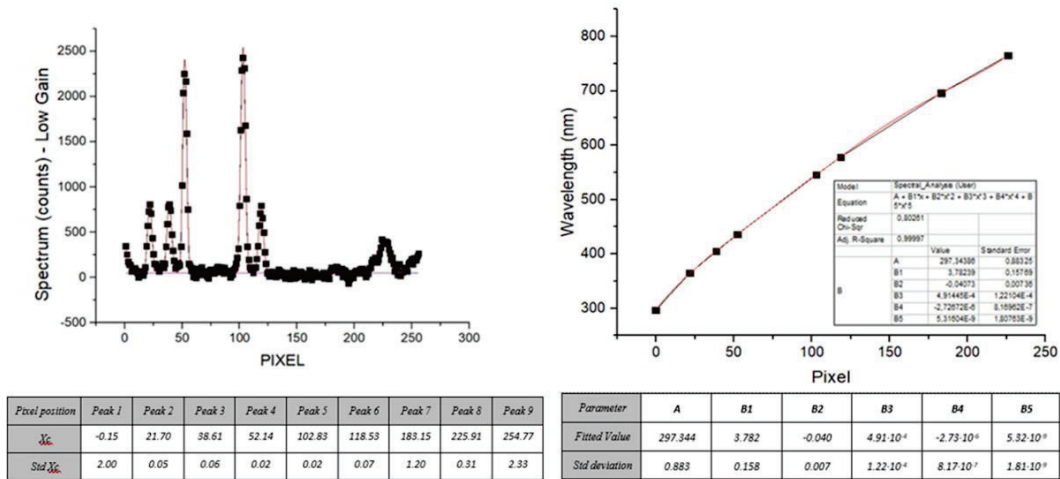| Parameter	A	B1	B2	B3	B4	B5
Fitted Value	297.344	3.782	-0.040	$4.91 \cdot 10^{-4}$	$-2.73 \cdot 10^{-6}$	$5.32 \cdot 10^{-9}$
Std deviation	0.883	0.158	0.007	$1.22 \cdot 10^{-4}$	$8.17 \cdot 10^{-7}$	$1.81 \cdot 10^{-9}$

Figure 16. Analyzed spectrum by (14). Characteristic curve to obtain the main parameters with (15).

The final results of this calibration for the spectral response of the mini-spectrometer are shown in the next table. Then, it is possible to compare these results with the provided ones from the manufacturer and determine the maximum displacement on the wavelength values, the highest variation is from pixel-0 which could be expected because of the difficulty of measuring the first pixel, even more if it is out of the wavelength range considered for this device.

Table 1. Results of the calibration for the spectral response of the mini-spectrometer.

Xc (pixel)	-0.15	21.70	38.61	52.14	102.83	118.53	183.15	225.91
Lambda (nm)	296.78	364.69	405.34	435.38	546.22	577.99	670.50	765.18

4.3 Spectral thermal response function calibration

The goal of this analysis carried out on the experimental data is to obtain a mathematical expression which allows to related the variation of the wavelength displacement with the temperature. This analysis has been done by choosing 7 different temperature values, covering the thermal range previously evaluated in the thermal calibration tests:

- 44.34 °C, 34.98 °C, 25.19 °C, 0.60 °C, -51.33 °C, -103.24 °C, -131.14 °C

By using Gaussian equation, it is obtained the position of the peaks based on the lambda values given by NIST pattern. As well as it was done in the previous section, with these results and using (15), a fitting is done in order to obtain the characteristic values of the parameters depending on the temperature. Then, it was possible to stablish a relation between the temperature and each one of the characteristic parameters from **¡Error! No se encuentra el origen de la referencia.**. With all these information, figure 17 shows the corresponding curves for each of the parameters versus the temperature in order to find a mathematical expression for describing the thermal dependence.
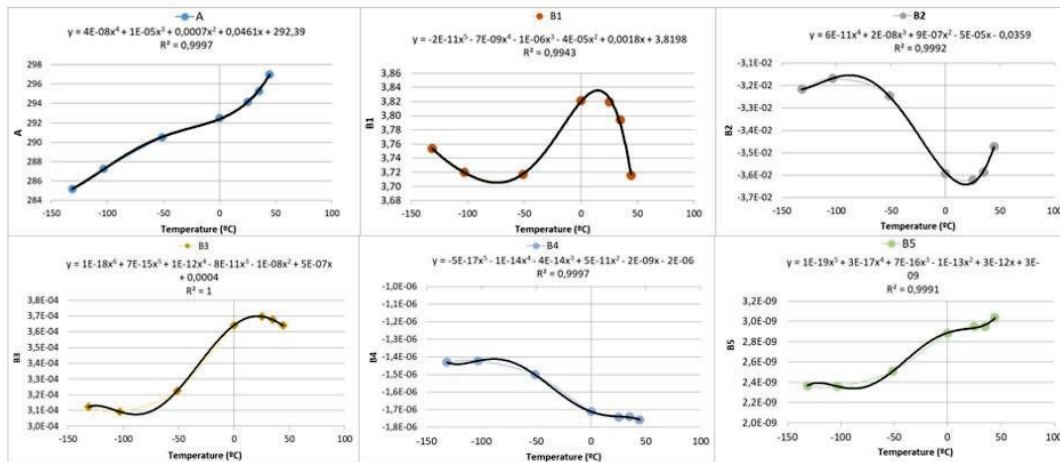
Figure 16. Analyses from each characteristic parameter depending on the temperature.

After analysed all the scenarios, the reference value of the temperature to compare the rest of the data has been T = 35 ºC. Figure 17 shows, once the data has been normalised to this reference value, the displacement on the pixel position of the peak in terms of the temperature.
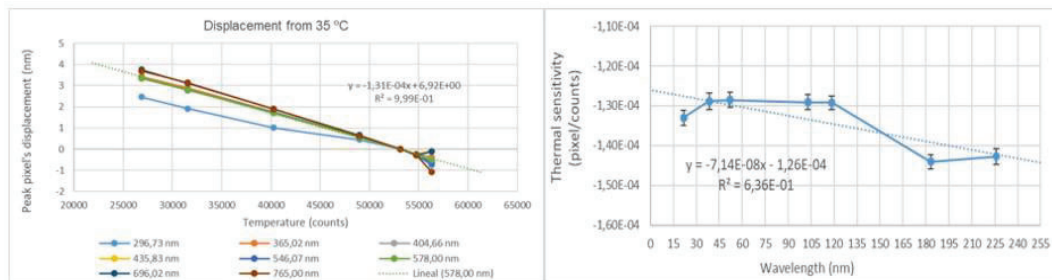

Figure 17. Displacement on the pixel position (left). Thermal sensitivity from the spectral thermal response correction found (right).

Finally, the mathematical expression which will allow to correct the spectral thermal displacement, give us an idea about the thermal sensitivity (wavelength/temperature) per pixel. This equation is:

$$\Delta \frac{nm}{°C} = -7.14 \cdot 10^{-8} - 1.26 \cdot 10^{-4} \tag{26}$$

Results of these corrections could be seen in the next **¡Error! No se encuentra el origen de la referencia.**. The first plot corresponds to 2 spectra at different temperature, where the displacement on the pixel where the peaks are, is remarkable. On the other hand, the second plot corresponds to the same two spectrums where **¡Error! No se encuentra el origen de la referencia.** has been applied and the data has been corrected successfully.
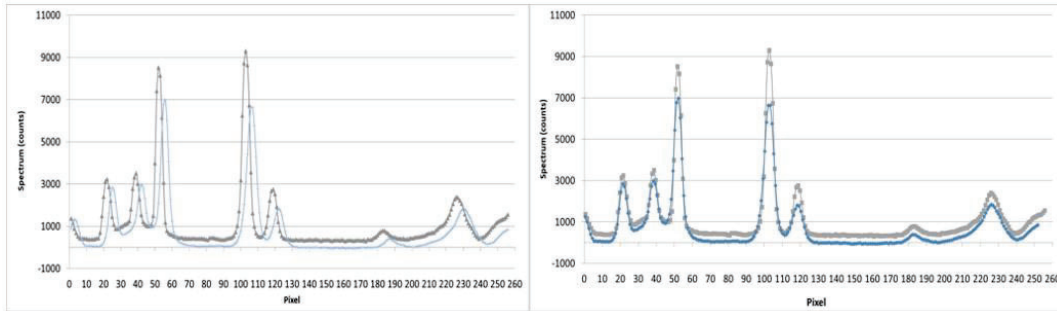
Figure 18. Same spectra at different temperatures, the one in the left is from the experimental data where a displacement in the pixel position of the peaks are remarkable. The picture in the right side shows the effect on the spectral thermal response correction after apply over the data the obtained equation (26).

4.4 Thermal response function calibration

Figure 19 shows the results of the TRF analysis explained in section 3.3. It is shown the experimental data analyzed and the corresponding TRF fitting by using (13). The data had been normalized to the work temperature average value, 51980 counts. On the other hand, the signals measured by each photo-sensor are saturated for almost all the optical channels when the measurement is done with high gain configuration.
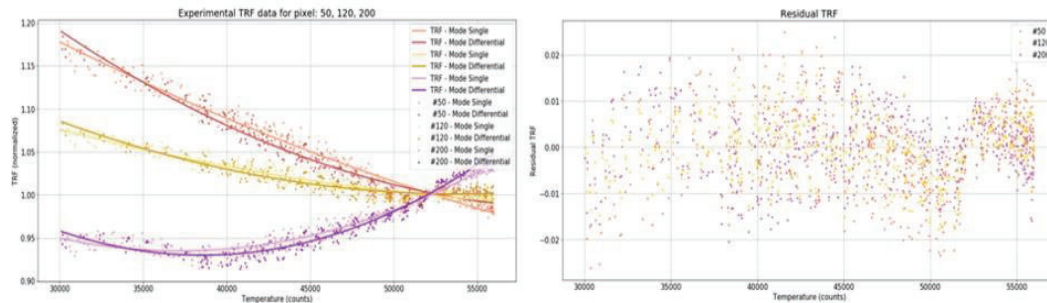
Figure 19. Experimental data and TRF fitting from 3 different pixels measuring under nominal gain and both acquisition modes, single and differential (left). Residual from the fitting (right).

It can be assumed that there are barely any thermal variations between measuring with nominal gain and high gain configurations, as has happened before in other similar test carried out under similar conditions by using the same equipment. Considering all this, is possible to use the same results for both gains.

4.5 Angular response function calibration

As it was explained in section 3.6, these results have been obtained by measuring the angular response of the signal from each pixel under normal light incidence whereas the incidence angle varies. Due to the large number of pixels analyzed and the similar behavior between them, it has been decided to use a single result to fit every pixel analyzed with (22). Figure 20 shows the ARF experimental data from pixel #50 (blue) and the ARF calibration model (orange).
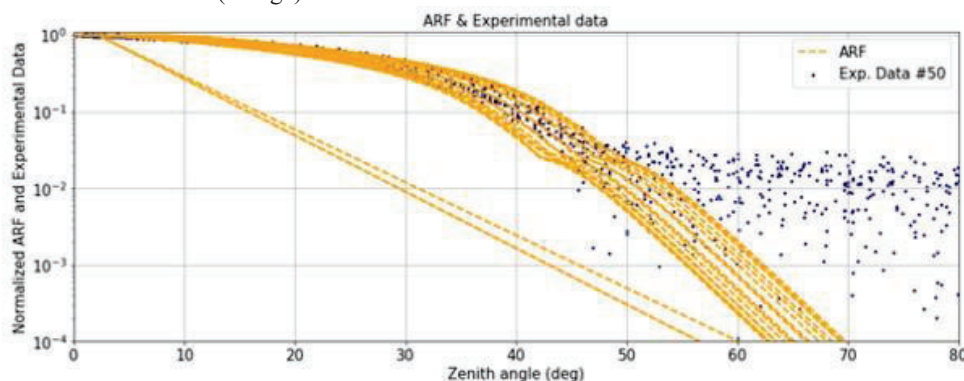

Figure 20. Experimental data from pixel #50 (blue) and the ARF mathematical model (orange), in logarithmic scale and normalized results.

Figure 21 shows the results from the ARF analysis in terms of the residual obtained from the fitting (left) and the relative error (right). There, it is also possible to evaluate the level of ARF noise.
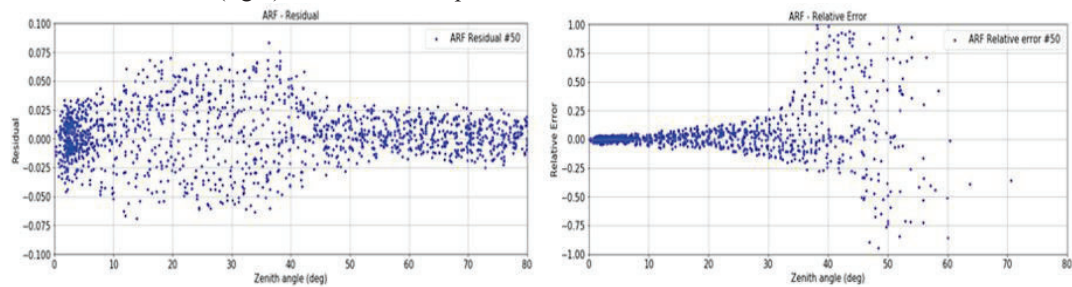

Figure 21. Residual from the fitting (left) and the relative error (right).

4.6 Mean throughput calibration

The experimental data are fitted to (24) in order to obtain the amplitude value, then, these values are represented and analyzed versus the irradiance level by a straight-line fitting, where the slope is the responsivity. We have to take into account the presence of statistical uncertainties in the measures, including the uncertainty of the amplitude of the signal and, on the other hand the uncertainty in the irradiance measured by the spectra-radiometer.

To obtain the responsivity it is needed to transform the pixel to the corresponding wavelength value by using next equation 27. Where it is possible to transform the 'pixel number' into their corresponding value of wavelength (nm).

$$Pixel = 3.00004 \cdot 10^2 + 32.2257 \cdot x - 1.75695 \cdot 10^{-2} \cdot x^2 + 1.40452 \cdot 10^{-4} \cdot x^3 - 5.64123 \cdot 10^{-7} \cdot x^4 + 8.20048 \cdot 10^{-10} \cdot x^5 \tag{27}$$

It is also need to evaluate them versus the corrected irradiance values for each irradiance level and wavelength range of the pixel. So it is, there will be four corrected irradiance values per pixel to represent the obtained amplitude of the signal value. Figure 22 shows the signal measured by the mini-spectrometer versus the wavelength and the corresponding level of irradiance in each of the four scenarios analyzed.
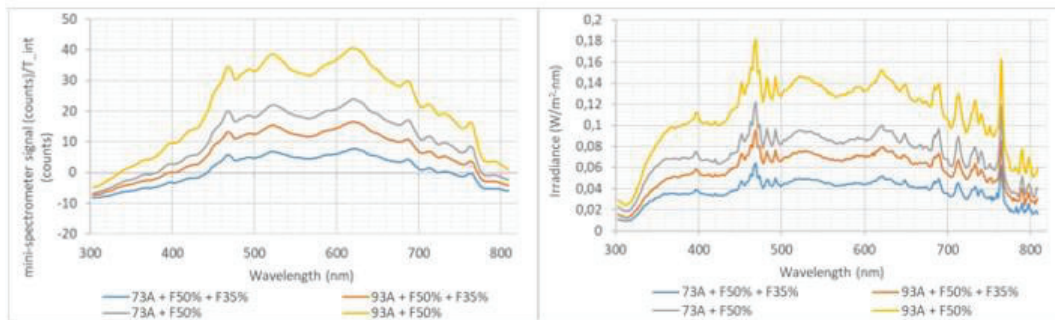

Figure 22. Signal of the mini-spectrometer (left) and the corrected irradiance levels (right).

Finally, it is possible to stablish a linear relation between the irradiance level and the amplitude signal measured. Figure 23 shows an example of the slope from 3 different pixels analyzed, and the result from all the pixels evaluated. It has to be considered the spectral width of the mini-spectrometer, 9 nm per pixel.
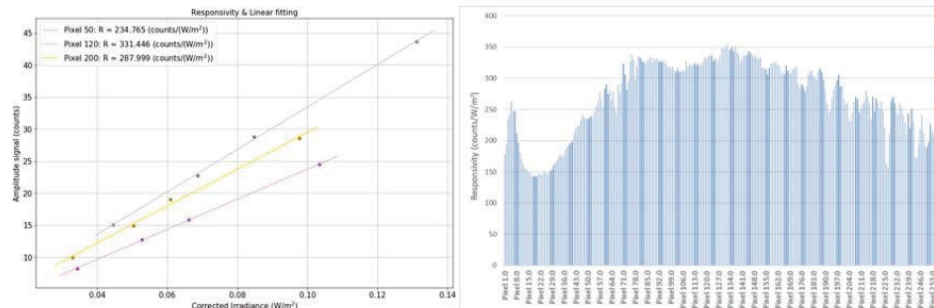

Figure 23. Results from 3 pixels (left) and mean throughput values from all the pixels (right).

5. CONCLUSIONS

The calibration procedure of the FM SIS mini-spectrometer has been presented. In addition, the results of the characterization of the mini-spectrometer instrument installed on the Solar Irradiance Sensor (SIS'22) of the ExoMars'22 Radiation and Dust Sensor for Meteo package (RDM) are discussed.

The procedure is divided into the different calibration tests needed to determine and understand the electrical signal from the device under study. These tests are separated into their mean characteristic parameters: thermal, spectral, angular and mean throughput calibration tests.

It has been explained some improvements comparing to previous calibrations in terms of thermal dependences, the characterization of the 'blocking zone' by defining a mathematical model of ARF to study direct and diffuse light conditions.

The radiation environment might have an influence in the response of the devices. The mini-spectrometer covered and working in dark conditions will act as a displacement damage sensor installed in the SIS. This will be fundamental to measure the level of high-energy radiation received by the detectors and compensate for its influence in the detector.

However, the use of this calibration model must be applied together with atmospheric models, straylight effects or different methods to evaluate the real conditions on the surface of Mars.

REFERENCES

[1] Guerrero, H.: Development of miniaturized instrumentation for Planetary Exploration and its application to the Mars MetNet Precursor Mission. In: EGU General Assembly Conference Abstracts 2010,Vol. 12 p. 13330

[2] Apéstigue,V., et al.: DREAMS-SIS: A Miniature Instrument for the Measurement of Atmospheric Optical Depth on ExoMars 2016 EDM. International Workshop on Instrumentation for Planetary Missions – IPM-2014. Greenblet. Maryland (2014)

[3] Esposito, F., Debei, S., Bettanini, C., Molfese, C., Arruego Rodriguez, I., Colombatti, G., Harri, A.M., Montmessin, F., Wilson, C., Aboudan, A., others: The DREAMS Experiment of the ExoMars 2016 Mission for the study of Martian environment during the dust storm Season. In: Eighth International Conference on Mars 2014, p. 1246

[4] Arruego, I., Apéstigue, V., Jiménez, J.J., Martínez-Oter, J., Álvarez-Ríos, F.J., González-Guerrero, M., Rivas, J., Azcue, J., Martín, n., I., Toledo, D., others: DREAMS-SIS: The Solar Irradiance Sensor on-board the ExoMars 2016 lander. Advances in Space Research 60(1), 103-120 (2017).

[5] Toledo, D., Arruego, I., Apéstigue, V., Jiménez, J.J., Gómez, L., Yela, M., Rannou, P., Pommereau, J.-P.: Measurement of dust optical depth using the solar irradiance sensor (SIS) onboard the ExoMars 2016 EDM. Planetary and Space Science 138, 33-43 (2017)

[6] http://mars.nasa.gov/mars2020/mission/rover/ Accessed August 2022

[7] Ápestigue,V., Gonzalo,A., Jiménez,J.J., et al. Radiation and Dust Sensor for Mars Environmental Dynamic Analyzer Onboard M2020Rover. Sensors2022,22(8),2907;https://doi.org/10.3390/s22082907

[8] Lemmon, M.T.; Wolff, M.J.; Bell, J.F.; Smith, M.D.; Cantor, B.A.; Smith, P.H.; Dust aerosol, clouds, and the atmospheric optical depth record over 5 Mars years of the Mars Exploration Rover mission. 2015. Icarus. Vol 251: 96 –111. https://doi.org/10.1016/j.icarus.2014.03.029.

[9] Rodriguez-Manfredi, J. A., et al. (2021). The Mars Environmental Dynamics Analyzer, MEDA. A suite of environmental sensors for the Mars 2020 mission. Space science reviews, 217(3), 1-86.

[10] Newman, C.E. et al. The dynamic atmospheric and aeolian environment of Jezero crater, Mars, Science Advances (in press).

[11] Jiménez,J.J., J Álvarez,F., Gonzalez-Guerrero,M. et al. Calibration OGSEs for multichannel radiometers for Mars atmosphere studies. CEAS Space J10,127–145(2018).https://doi.org/10.1007/s12567-018-0194-8

[12] Wyatt, C.L.; Radiometric Calibration: Theory and Methods. Academic Press Inc, New York (1978).

[13] Wyatt, C.L.; Electro-optical System Design for Information Processing. McGraw-Hill, New York (1991).

[14] Marquez, J.M.A.; Bohórquez, M.A.M.; Garcia, J.M.; Nieto, F.J.A.; A new automatic system for angular measurement and calibration in radiometric instruments. Sensors 10(4), 3703-3717 (2010)

[15] Tansock, J.; Bancroft, D.; Butler, J.; Cao, C.; Datla, R.; Hansen, S.; Helder, D.; Kacker, R.; Latvakoski, H.; Mylnezak, M.; et al.; Guidelines for radiometric calibration of electro-optical instruments for remote sensing. (2015). http://doi.org/10.6028/NIST.HB.157

[16] Tansock, J.J.; Hansen, S.; Paskett, K.; Shumway, A.; Peterson, J.; Stauder, J.; Gordley, L.L.; Wang, Y.; Melbert, M.; Rusell, J.M.; et al.; SABER ground calibration. Int. J. Remote sens. 24(2), 403-420 (2003).

[17] Datla, R.; Shao, X.; Cao, C.; Wu, X.; Comparison of the calibration algorithms and SI traceability of MODIS, IIRS, GOES, and GOES-R ABI sensors. Remote Sens. 8(2), 126 (2016).

[18] Gras, A.; Fernandez-Marin, J.M.; Aguilar, J.M.; Robert, P.; Baur, C.; Multi-Source Solar Simulator Characterization for Establishing AM0 Equivalent Conditions. In: 8th European Space Power Conference, September 2008. ESA Special Publication, p. 92